ADVANCED FUNCTIONAL MATERIALS
www.afm-journal.de

One-Step Self-Assembly Fabrication of High Quality $Ni_xMg_{1-x}O$ Bowl-Shaped Array Film and Its Enhanced Photocurrent by Mg,$^{2+}$ Doping

*Yan Zhao, Linfeng Hu, Shangpeng Gao, Meiyong Liao, Liwen Sang, and Limin Wu**

A series of high quality $Ni_xMg_{1-x}O$ bowl-shaped array films are successfully prepared by a simple one-step assembly of polystyrene colloidal spheres and metal oxide precursors at oil–water interface, and further used to fabricate nanodevices. The doping of Mg^{2+} can greatly enhance the current and spectrum responsivity of NiO film-based nanodevice. The maximum R_λ value of these bowl-shaped $Ni_xMg_{1-x}O$ film-based devices measured in the study shows 4–5 orders of enhancement than the previously reported $Ni_xMg_{1-x}O$ film at equal doping.

1. Introduction

Nickel oxide (NiO) is a well-known wide-bandgap semiconductor with unique properties and has attracted wide attention due to its potential applications in electrode materials for dye-sensitized solar cells, catalysts, electrochromic display devices, and electrochemical supercapacitors.[1] For example, the high resistivity of NiO makes it promising for photodetector in terms of low dark current.[2] The insulating properties of NiO also offer the advantage for conductivity tailoring by doping.[3] However, difficulties have been encountered in the commercial exploitation of NiO film due to its phase separation, lattice mismatch with doping atoms.[4] And there is far limited characterization of the optoelectronic properties and mechanistic function of metal ions doped NiO nanofilms. Therefore, it is of particular importance to construct metal ions doped NiO nanostructures with improved optical and electrical properties suitable for the uses in optoelectronic and microelectronic devices. Although many methods, such as radio frequency magnetron sputtering,[5] electron beam evaporation,[6] chemical bath deposition,[7] and electrochemical deposition[8] can be used to fabricate NiO and metal ions doped NiO films, they usually involve either expensive equipments or complex fabrication procedures.[9] Recently, the bottom-up self-assembly has attracted considerable interest as a potential alternative to conventional top-down processes for the scalable, low-cost syntheses of nanoporous solid structures.[10] Monolayer, bilayer, or multilayer colloidal film-based nanodevices have been reported by the oil–water interfacial self-assemble strategy.[11,12] Moreover, this method can be further extended for fabrication of high performance porous nanofilm-based optoelectronic devices due to large surface-to-volume ratio and efficient light harvest.[13] Nevertheless, the whole process seems to be complicated, including the self-assembly and drying of polymer colloidal spheres, the infiltration of metal oxide precursors, the calcination and so on. Accordingly, a more facile method for fabrication of well-ordered pore nanofilms for optoelectronic nanodevices is highly desired.

In this study, we present the first $Ni_xMg_{1-x}O$ bowl-shaped array film by one-step self-assembly of monodisperse polystyrene (PS) colloid spheres and metal oxide precursors at oil-water interface and further construct the array film-based optoelectronic device. Our approach at least has several prominent features: i) Unlike previous fabrication procedures, the crystal nuclei of the metal oxide precursors can directly self-assemble on the bottom surfaces of the organizing PS spheres to form a bowl-shaped nanofilm. This greatly decreases the steps of fabrication. ii) Through this simple process, it is easy to realize the doping of other metal ions, which may tune the optoelectronic properties of the semiconducting film-based nanodevices. iii) Compared with undoped NiO films, doping of Mg^{2+} significantly enhances the current and spectrum responsivity of NiO film-based nanodevice.

2. Results and Discussion

2.1. Fabrication and Structure of $Ni_xMg_{1-x}O$ Bowl-Shaped Array Films

Scheme 1 briefly describes the fabrication procedures of bowl-shaped $Ni_xMg_{1-x}O$ nanofilm and its corresponding optoelectronic device. Pure $Ni(NO_3)_2 \cdot 6H_2O$, or the mixture of $Mg(NO_3)_2 \cdot 6H_2O$ and $Ni(NO_3)_2 \cdot 6H_2O$ (mole ratios of Mg/(Mg+Ni): 0.05, 0.1, 0.2,

---

Dr. Y. Zhao, Dr. L. Hu, Dr. S. Gao, Prof. L. Wu
Department of Materials Science and State Key
Laboratory of Molecular Engineering of Polymers
Fudan University
Shanghai 200433, P.R. China
E-mail: lmw@fudan.edu.cn
Dr. M. Liao
Optical and Electronic Materials Unit
National Institute for Materials Science (NIMS)
Tsukuba, Ibaraki 305-0044, Japan
Dr. L. Sang
International Center for Materials Nanoarchitectonics (MANA)
National Institute for Materials Science (NIMS)
Tsukuba, Ibaraki 305-0044, Japan

DOI: 10.1002/adfm.201500071

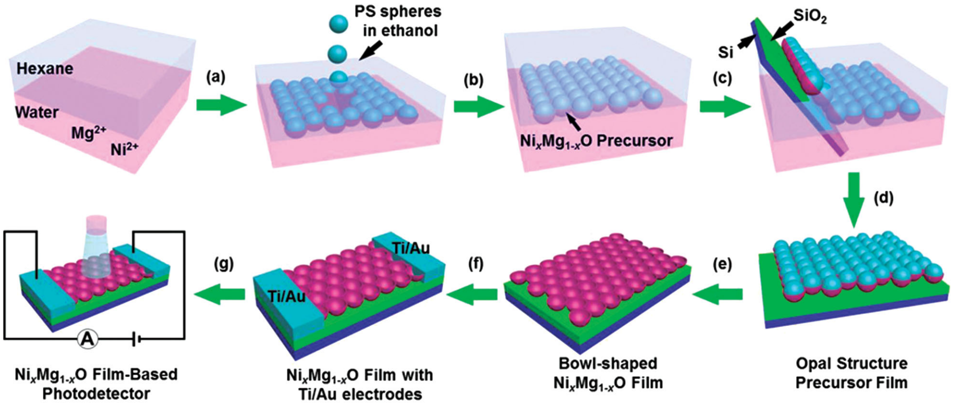

Scheme 1. Schematic illustration of the fabrication procedure of bowl-shaped $Ni_xMg_{1-x}O$ array nanofilm and its optoelectronic device. a,b) Hexane–water interfacial self-assembly procedure. c,d) Lift-up approach. e) Heat treatment process. f) Vacuum evaporation. g) $Ni_xMg_{1-x}O$ nanofilm device.

and 0.3) was dissolved in water as the aqueous phase. Hexane was then slowly added to produce a hexane/water interface. When the PS dispersion was injected to the interface, the PS colloidal spheres were gradually trapped at the interface to form closely packed nanofilm. Meanwhile, the metal oxide precursors from the aqueous phase were assembling on the bottom surfaces of PS spheres. The assembled PS colloidal film was aged at the interface for another 5 h to be immersed by enough metal oxide precursors, and then transferred onto a SiO_2/Si substrate, followed by drying at 60 °C and calcination at 500 °C to produce well-ordered bowl-shaped $Ni_xMg_{1-x}O$ monolayer films.

Figure 1a presents the typical scanning electron microscopy (SEM) image of the metal oxide precursor/PS hybrid monolayer film which was prepared from PS and the mixture of $Mg(NO_3)_2{\bullet}6H_2O$ and $Ni(NO_3)_2{\cdot}6H_2O$ (mole ratio, 0.05:0.95). The hybrid spheres are closely packed, indicating the high-quality of the hybrid monolayer film with a thickness equal to the diameter (650 nm) of PS spheres (see the inset of Figure 1a). After calcination, a well-ordered, hexagonally arranged bowl-shaped $Ni_{0.95}Mg_{0.05}O$ nanofilm has been obtained (Figure 1b). The bowl-shaped array film can be further verified from the cross-sectional image in the inset of Figure 1b. The pore size and density can be easily controlled by the size of the starting PS particles. The aging time of PS colloidal film at the interface was a trick. A shorter aging time (e.g., less than 30 min) led to unconnected nanonet with a low height (Figure S1, Supporting Information). After 2 h, the nanofilms became thicker and interconnected. When the aging time was increased to 5 h, a well-ordered bowl-shaped film was produced. In addition, too low precursor concentration (e.g., below 0.10 mol L^{-1}) caused a thin and discontinuous network structure, while too high concentration (e.g., 0.32 mol L^{-1}) produced a shrinkage of the hole-wall (Figure S2, Supporting Information).

Similar periodic bowl-shaped structures of NiO, $Ni_{0.9}Mg_{0.1}O$ and $Ni_{0.8}Mg_{0.2}O$ monolayer films can also be fabricated (**Figure 2**a–c). The optical images of these nanofilms deposited on quartz substrate and silicon substrate under natural light display that all of the nanofilms are uniform and semitransparent (Figure 2d,e), further indicating the high quality of these films. The typical atomic force microscopy (AFM) height profile (Figure 1c) of $Ni_{0.95}Mg_{0.05}O$ sample along the white line from X to Y (Figure 1d), indicates an average pore thickness of about 155 nm based on statistical examination of more than 20 nanopores and the surface root-mean-square roughness value of 51.2 nm.

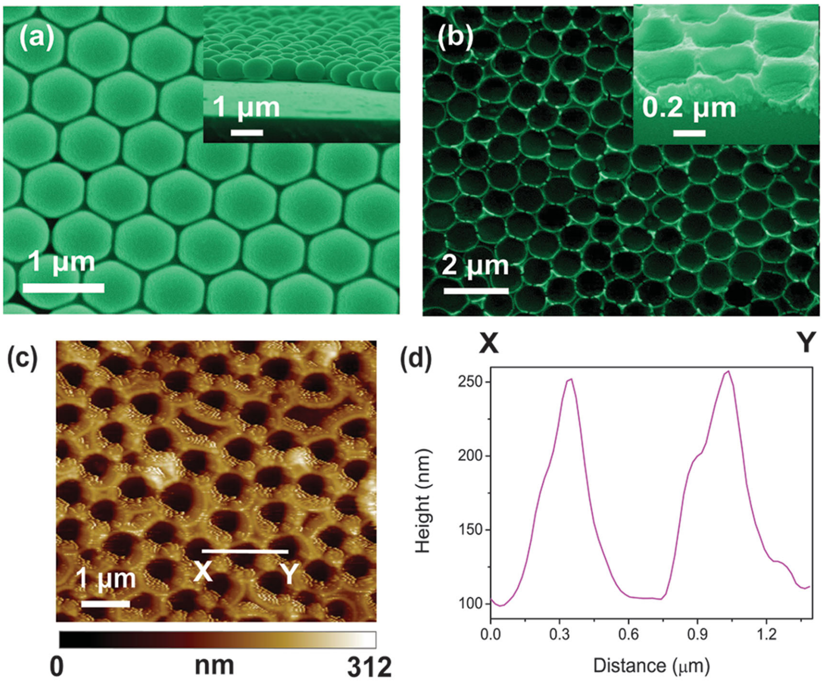

Figure 1. a) Typical surface SEM image of the PS/metal oxide hybrid nanofilm on a Si (100) substrate with the cross-sectional SEM image inserted. b) SEM image of bowl-shaped $Ni_{0.95}Mg_{0.05}O$ nanofilm with the cross-sectional SEM image inserted. c) Tapping-mode AFM image of the bowl-shaped $Ni_{0.95}Mg_{0.05}O$ nanofilm on a Si substrate. d) A height profile along the white line from X to Y.

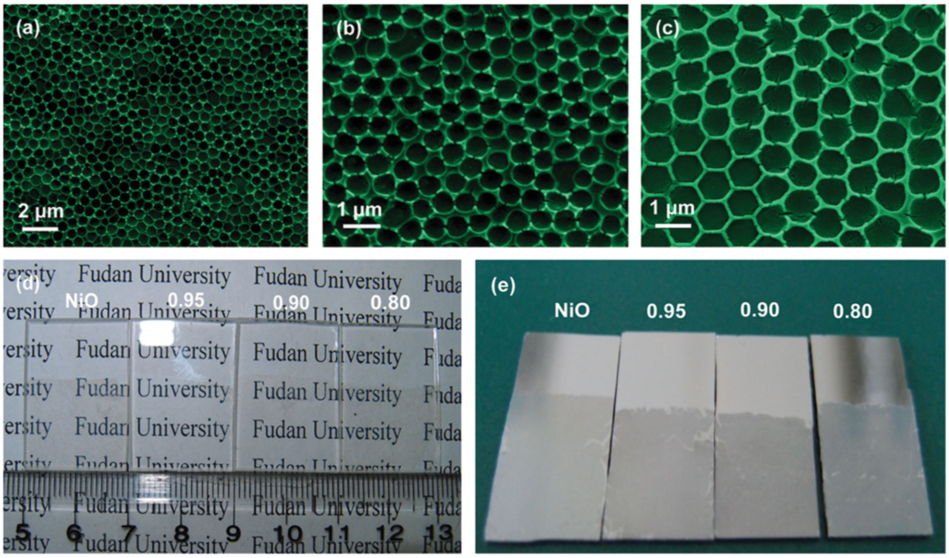

Figure 2. SEM images of a) NiO, b) $Ni_{0.9}Mg_{0.1}O$, c) $Ni_{0.8}Mg_{0.2}O$ monolayer films and their photographs deposited on various substrates: d) quartz substrates and e) silicon substrates.

The typical X-ray diffraction (XRD) patterns of powder samples shows strong and sharp diffraction peaks (**Figure 3**a), suggesting that the metal-oxides are highly crystallized. At $x = 1$, the experimental pattern agrees well with the standard pattern of NiO (JCPDS card 73-1519), which has a cubic structure with five major diffraction peaks of the (111), (200), (220), (311), and (222) planes. With the increase of Mg content from 0.05 to 0.3, the diffraction

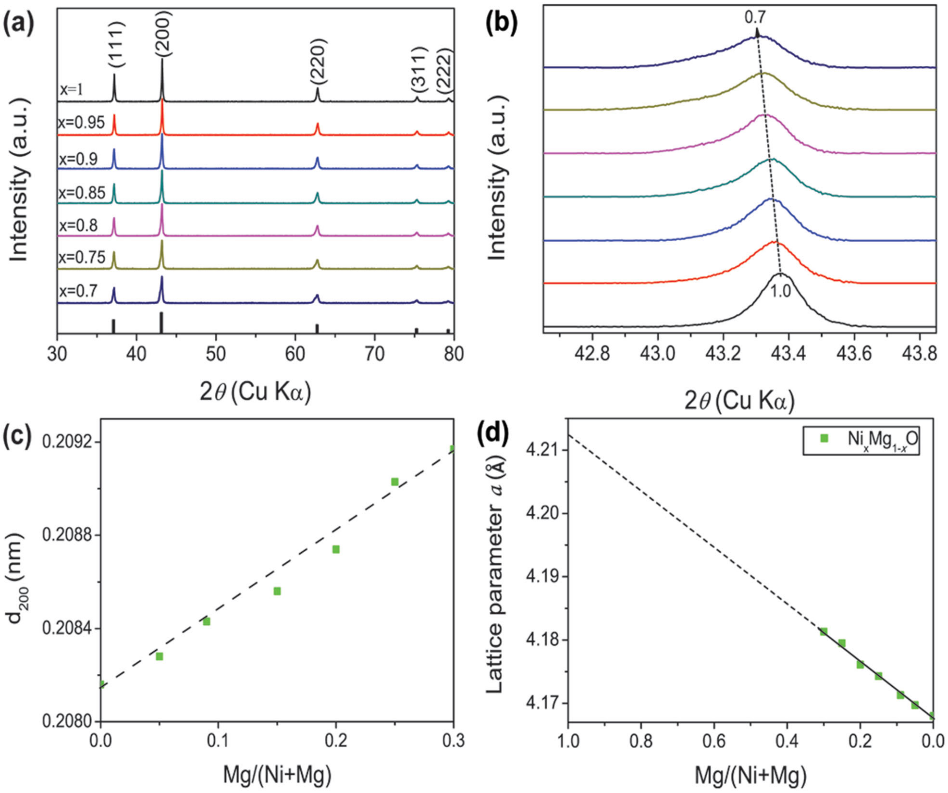

Figure 3. a) XRD patterns of $Ni_xMg_{1-x}O$ powders annealed at 500 °C. JCPDS 73-1519 pattern is shown for comparison (vertical lines). b) The XRD peaks of the (200) plane of $Ni_xMg_{1-x}O$ powder samples for various values of x. c) D_{200} spacing of $Ni_xMg_{1-x}O$ powder samples. d) The lattice parameter a of $Ni_xMg_{1-x}O$ powder samples as a function of Mg molar fraction.

peak of (200) of $Ni_xMg_{1-x}O$ powder samples shift toward lower 2θ values, and the interplanar spacings of $Ni_xMg_{1-x}O$ samples (200) planes increase (Figure 3b,c). The lattice parameter calculated from the XRD data has a linear relation with the mole ratio of Mg/(Mg+Ni) (Figure 3d), and the lattice constant increases from 4.168 to 4.181 Å as the mole ratio of Mg/(Mg+Ni) rises from 0 to 0.3. By extrapolating the solid line to a mole ratio of 1 for Mg/(Mg+Ni), a lattice constant of 4.211 Å can be obtained which is very close to the experimental lattice constant of pure MgO (4.211 Å, JCPDS card 87-0652). This agreement obeys the Vegard's Law[14] and confirms the formation of homogeneous solid solution samples. The more detailed elemental composition and the oxidation state of the obtained $Ni_xMg_{1-x}O$ nanofilms are further characterized by X-ray photoelectron (XPS) measurements and the corresponding results are presented in Figure S6, Supporting Information. These data show that the surface of the obtained $Ni_xMg_{1-x}O$ nanofilm indeed contain Mg^{2+} and Ni^{2+}. The atomic ratios of Ni to Ni+Mg are calculated to be 0.946, 0.904, 0.804, and 0.763, corresponding to $Ni_{9.5}Mg_{0.05}O$, $Ni_{0.9}Mg_{0.1}O$, $Ni_{0.8}Mg_{0.2}O$, and $Ni_{0.7}Mg_{0.3}O$ films, respectively, which are very close to the source material ratio (Table S1, Supporting Information).

2.2. Optoelectronic Properties of $Ni_xMg_{1-x}O$ Bowl-Shaped Nanofilms

As illustrated in **Figure 4**a, a novel nanodevice has been successfully constructed based on this bowl-shaped array nanofilm, through the deposition of Ti (100 nm)/Au (100 nm) electrode on the $Ni_xMg_{1-x}O$ film using photolithography, electron-beam deposition, and the lift-off process.[15] The typical SEM image of the $Ni_{0.95}Mg_{0.05}O$ film-based nanodevice (Figure 4b) shows that the nanobowl structure is well maintained with few tiny holes, which might be caused by the stripping in the process of lithography. Figure 4c reveals the *I–V* curves of the device illuminated with radiation of different wavelengths and under dark condition, respectively. It can be seen that the device shows a low dark current of 66 pA at an applied voltage of 10 V, and the photoresponsivity just shows very slight change when the wavelengths of the light sources are 550 nm (252 μW cm^{-2}) and 450 nm (322 μW cm^{-2}). When this device was illuminated by 350 nm (152 μW cm^{-2}) and 320 nm (11.3 μW cm^{-2}), the currents increase drastically to 147 and 253 pA, respectively. Therefore, the present bowl-shaped $Ni_{0.95}Mg_{0.05}O$ array film-based nanodevice is much more sensitive to UV light than visible light, indicating a high spectral selectivity. This can be attributed to that the photogenerated carriers significantly increase the conductivity when the nanofilm is illuminated by photons with an energy larger than its band gap. The approximately symmetrical feature of the plots indicates the ohmic contact between the electrodes and the porous monolayer film. Similar *I–V* curves were also measured for bowl-shaped NiO, $Ni_{0.9}Mg_{0.1}O$ and $Ni_{0.80}Mg_{0.20}O$ array film-based nanodevices (Figure S3, Supporting Information).

Figure 4d further compares the *I–V* characteristics of NiO, $Ni_{0.95}Mg_{0.05}O$, $Ni_{0.90}Mg_{0.10}O$, and $Ni_{0.80}Mg_{0.20}O$ film-based devices upon 320 nm light illumination at an applied voltage of 10 V. Interestingly, the photocurrent increases from 129 pA for pure NiO array nanofilm to 253 pA for $Mg_{0.05}Ni_{0.95}O$, as shown in **Table 1**, and then rapidly increases to 703 pA for $Mg_{0.10}Ni_{0.90}O$ film-based nanodevices. Further increasing the Mg content to

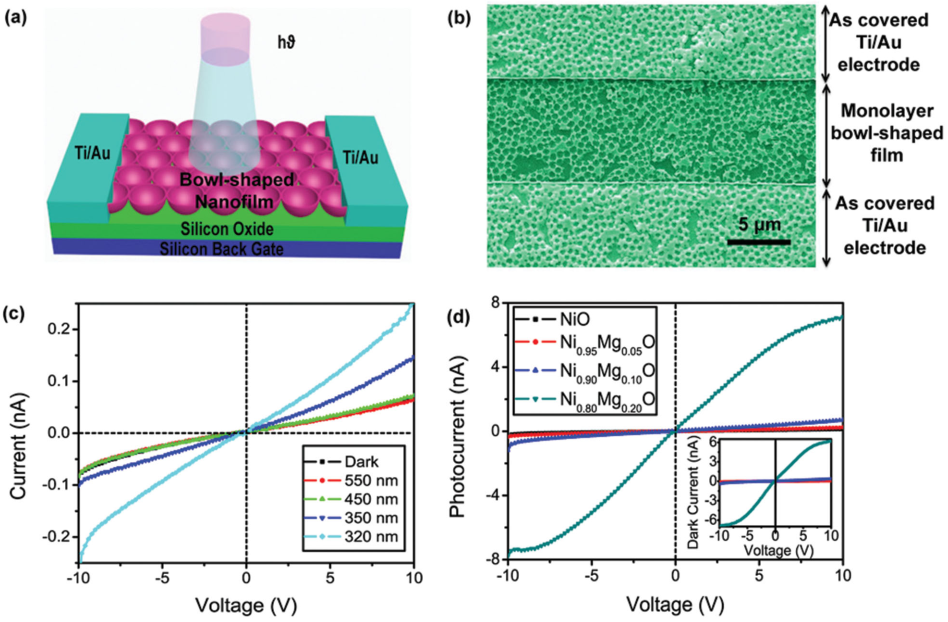

Figure 4. a) Schematics of the bowl-shaped array film-based nanodevice. b) A representative SEM image of the nanodevice. c) The *I–V* characteristics of the bowl-shaped $Ni_{0.95}Mg_{0.05}O$ nanofilm-based device illuminated with different-wavelength lights or under dark conditions. d) The *I–V* characteristics of NiO, $Ni_{0.95}Mg_{0.05}O$, $Ni_{0.90}Mg_{0.10}O$, and $Ni_{0.80}Mg_{0.20}O$ film-based devices upon 320 nm light illumination at an applied voltage of 10 V. Inset shows the *I–V* characteristics of NiO, $Ni_{0.95}Mg_{0.05}O$, $Ni_{0.90}Mg_{0.10}O$, and $Ni_{0.80}Mg_{0.20}O$ film-based devices under dark current at an applied voltage of 10 V.

Table 1. Comparison of the characteristic optoelectronic parameters of the $Ni_xMg_{1-x}O$ films obtained in the present work and previous reports.

Film-based photodetectors	Bias [V]	Photocurrent (I_{light})	Dark current (I_{dark})	$R\lambda$ [mA W^{-1}]	EQE	Ref.
$Ni_{0.54}Mg_{0.46}O$	10	–	1–10 nA	12	–	[6]
$Ni_{0.80}Mg_{0.20}O$	5	–	70 nA	0.147	–	[19]
NiO	10	129 pA	65 pA	570	221%	Present work
$Ni_{0.95}Mg_{0.05}O$	10	253 pA	66 pA	1250	485%	
$Ni_{0.90}Mg_{0.10}O$	10	723 pA	351 pA	2680	1040%	
$Ni_{0.80}Mg_{0.20}O$	10	7140 pA	6210 pA	6760	2620%	

0.2 can cause an enormous photocurrent increase to 7.14 nA. In fact, the doping of Mg^{2+} ions can also increase the dark current of these film devices (the inset of Figure 4d).

2.3. DFT Calculations

To illustrate the role of Mg^{2+} doping in the optoelectronic performance of NiO, density functional theory (DFT) calculations were carried out to investigate the mechanism. Density of states (DOS) analysis for pure NiO can be found in **Figure 5**a. A band gap is correctly present for NiO and Ni atoms show two kinds of spin states due to antiferromagnetic order. It is well known that standard DFT is a ground state theory and the DFT with the local density approximation (LDA) or the generalized gradient approximation (GGA) for exchange-correlation functional will underestimate the band gap.[16] A larger Hubbard U value in the DFT+U method tends to give a larger band gap and is often used to tune theoretical band gap semi-empirically in the literature. Strictly speaking, quasiparticle band structure as a one-particle excitation property should be treated in a more rigorous theoretical framework such as many-body perturbation theory.[16,17] Here we mainly focus on the electronic states analysis in this work and accept the fact that DFT-GGA will underestimate the band gap.

Although substitutional doping of Mg causes a slight variation in DOS, there is no additional electronic state appearing within the band gap (Figure 5b). That is to say, substitutional

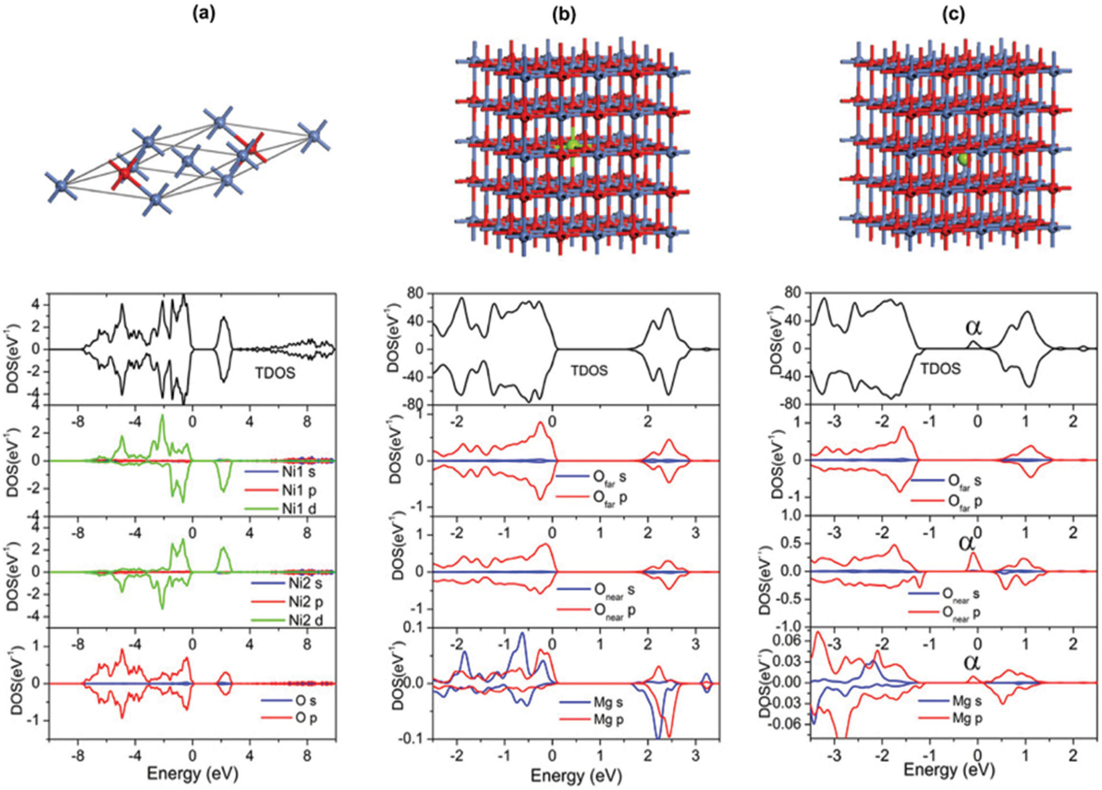

Figure 5. Structure, total density of states (TDOS), partial density of states for a) NiO, b) NiO with Mg dopant situated at substitutional site, and c) NiO with Mg dopant situated at interstitial site. For pure NiO, magnetic primitive cell is shown. Blue, red, and green spheres depict Ni, O, and Mg atoms, respectively. O_{far} and O_{near} denote oxygen atom far away from or near the Mg dopant, respectively. The energy level of highest occupied state is set to zero.

Mg cannot increase the carriers in NiO effectively. In contrast, the total DOS (Figure 5c) shows a new peak (indicated by α) appearing just below the unoccupied states. Partial DOS analysis (Figure 5c) indicates that this peak α appearing just below the unoccupied states is mainly contributed by the *p*-symmetry states of oxygen atoms adjacent to the interstitial Mg atom, whereas the oxygen atoms far away from the interstitial Mg atom do not have contribution to this feature. A peak also appears within similar energy range for *p*-symmetry states of Mg. So the electronic states represented by peak α in total DOS are caused by the interstitial doping of Mg and there is electron transfer from interstitial Mg to its adjacent O atoms. The occupied impurity level just below conduction band minimum caused by interstitial Mg corresponds to a typical n-type doping and will increase conduction electrons in NiO. Although it is more energetically favorable for Mg to occupy the substitutional site than to occupy the interstitial site, there is still small probability to form the interstitial Mg. Namely, with Mg content in NiO increasing to several percent or even several tens percent, a very small fraction of these Mg atoms will occupy the interstitial sites and these interstitial Mg atoms will increase n type carriers and thus explain the increasing electric current with larger Mg content as observed in the experiment.

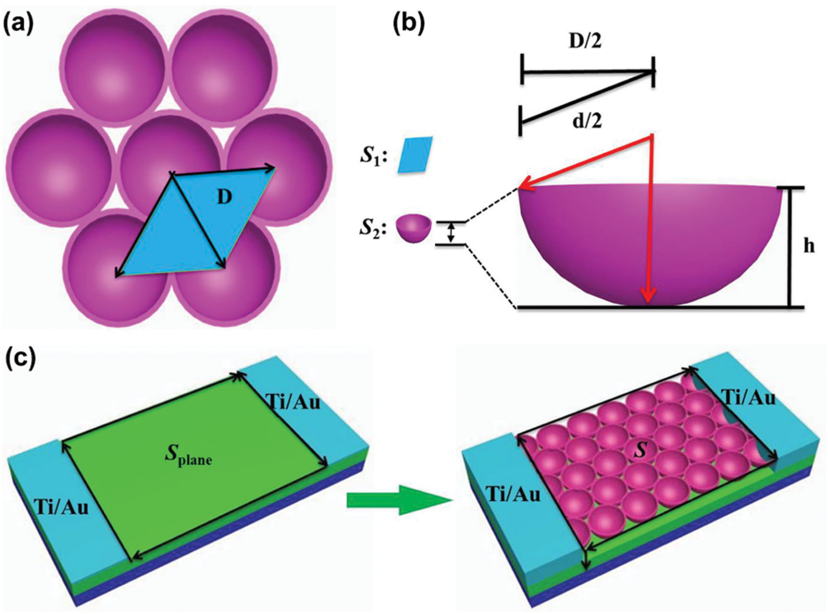

Figure 6. The bowl-shaped arrays models for calculating the surface area. a) Top view, b) sectional view, and c) the plane area (S_{plane}) and the surface area (S) models.

2.4. Spectrum Responsivity and External Quantum Efficiency

The spectrum responsivity (R_λ) and external quantum efficiency (EQE) are two critical parameters to determine the sensitivity for an optoelectronic device, which represent the ability to provide multiple photogenerated carriers per single incident photon.[18] R_λ is defined as the photocurrent generated per unit power of incident light on the effective area of a photodetector, and EQE as the number of electrons detected per incident photon. R_λ and EQE can be calculated in the following equations

$$R_\lambda = \frac{\Delta I_\lambda}{P_\lambda S} \tag{1}$$

$$\mathrm{EQE} = \frac{hcR_\lambda}{e\lambda} \tag{2}$$

where $\Delta I_\lambda = I_\lambda - I_\mathrm{d}$, I_λ is the photocurrent, I_d is the dark current, $P\lambda$ is the incident light intensity, S is the effective illuminated area, h is Planck's constant, c is the light velocity, e is the electronic charge, and λ is the incident light wavelength.

For our bowl-shaped structure nanodevice, S is different from the area between two electrodes (S_{plane}) because of the enlarged surface area of the bowl-shaped arrays (**Figure 6**). S_{plane} can be measured from the optical spectrum of the two electrodes of the nanofilm nanodevice (Figure S4, Supporting Information) and S is calculated to be 0.0133 mm^2 using the following equation (see the Supporting Information for details)

$$S = \frac{\sqrt{3}\left(2\sqrt{3}+\pi\right)}{2} \times S_{\text{plane}} \tag{3}$$

Thus, both the R_λ and EQE values of the present $Ni_xMg_{1-x}O$ array films can be calculated. As shown in Table 1, all the present bowl-shaped $Ni_xMg_{1-x}O$ array films display much higher the R_λ values than the previously reported $Ni_xMg_{1-x}O$ film-based devices, and show increasing R_λ as Mg^{2+} doping. The maximum R_λ value is 6.76 A W^{-1} at a bias of 10 V for $Ni_{0.8}Mg_{0.2}O$ film, corresponding to a high EQE value of 2620%. This value is even more than 60 000 times enhancement than the previously reported $Ni_{0.8}Mg_{0.2}O$ film with poor crystallinity.[19] This is probably because the large surface-to-volume ratio of the bowl-shaped array nanofilms can harvest more light and decrease the recombination of the photoexcited charges due to the multiple reflections of the bowl-shaped nanostructures,[20] as shown in Figure S5, Supporting Information, and the high crystal quality of the bowl-shaped nanofilms can also increase the number of photogeneration of carriers and facilitate oxygen adsorption and desorption at the $Ni_xMg_{1-x}O$ surface, reducing the resistance of the nanofilms.

3. Conclusion

We have demonstrated a simple assembly of PS colloidal spheres and metal oxide precursors at an oil/water interface to fabricate high-quality bowl-shaped $Ni_xMg_{1-x}O$ ($0.7 \le x \le 1$) array films. These well-ordered bowl-shaped array films can be further constructed for optoelectronic devices. The doping of Mg^{2+} ions significantly enhances the photocurrents of the $Ni_xMg_{1-x}O$ film-based devices. And the more the Mg^{2+} doping, the higher the photocurrent is. Meanwhile, the R_λ and EQE values also increase with the Mg^{2+} doping. The maximum R_λ value of these bowl-shaped $Ni_xMg_{1-x}O$ film-based devices measured in the study shows 4–5 orders of enhancement than the previously reported $Ni_xMg_{1-x}O$ film at equal doping. The present method should be versatile and can be readily extended to fabricate other pure metal oxide- or doped metal oxide-based bowl-shaped array films for the applications of high performance photodetectors, solar cells, and so on.

4. Experimental Section

Preparation of PS Colloidal Spheres and Bowl-Shaped Monolayer Film: Monodisperse colloidal PS spheres with size of 650 nm was synthesized by our previous method.[21] The metal oxide precursor/PS hybrid films were fabricated through an oil–water interfacial self-assembly method, and then transferred onto some SiO_2 (200 nm)/Si substrates. These hybrid colloidal films were dried at 60 °C for 6 h and then annealed at 500 °C for 2 h to produce bowl-shaped $Ni_xMg_{1-x}O$ monolayer films.

Construction of Bowl-Shaped $Ni_xMg_{1-x}O$ Monolayer Film-Based Nanodevices: The as-transformed $Ni_xMg_{1-x}O$ films were transported to an electric gun deposition system (ULVAC UEP-3000–2C). The Ti/Au (100 nm/100 nm) microelectrodes (distance ≈ 10 µm) were patterned on the top of each nanofilm using optical lithography with the assistance of a pre-designed mask and electron-beam deposition process.

Optoelectronic Measurements and DFT Calculation: Optoelectronic nanodevices were then constructed from these bowl-shaped $Ni_xMg_{1-x}O$ array nanofilms (see the Supporting Information for details). The current–voltage (*I*–*V*) characteristics of the nanodevices were measured using an Advantest Picoammeter R8340A and a dc voltage source R6411. The incident light power was calibrated using an UV enhanced Si photodiode. The calculation was based on plane wave pseudopotential method within DFT.[16,17,22] CASTEP code in Materials Studio 6.1 package was employed.

Supporting Information

Supporting Information is available from the Wiley Online Library or from the author.

Acknowledgements

Y.Z. and L.H. contributed equally to this work. Financial support was received from the National Natural Science Foundation of China (Grant Nos. 51133001, 21374018, and 51372040), National “863” Foundation (2013AA031801), Innovation Program of Shanghai Municipal Education Commission (14ZZ003), Science and Technology Foundation of Ministry of Education of China (20110071130002), and Science and Technology Foundation of Shanghai (12nm0503600, 13JC1407800).

Received: January 7, 2015
Revised: March 24, 2015
Published online: April 15, 2015

---

[1] a) L. Li, E. A. Gibson, P. Qin, G. Boschloo, M. Gorlov, A. Hagfeldt, L. Sun, *Adv. Mater.* **2010**, *22*, 1759; b) L. Tong, A. Iwase, A. Nattestad, U. Bach, M. Weidelener, G. Götz, A. Mishra, P. Bäuerle, R. Amal, G. G. Wallace, A. J. Mozer, *Energy Environ. Sci.* **2012**, *5*, 9472; c) V.-D. Dao, LiudmilaL. Larina , K.-D. Jung, J.-K. Lee, Ho-Suk Choi, *Nanoscale* **2014**, *6*, 477; d) M. G. James, B. Maryline, K. Michael, T. Stefanie, O. Sascha, H. Leif, *J. Am. Chem. Soc.* **2012**, *134*, 19322; e) G. Cai, J. Tu, J. Zhang, Y. Mai, Y. Lu, C. Gu, X. Wang, *Nanoscale* **2012**, *4*, 5724; f) Q. Lu, M. W. Lattanzi, Y. Chen, X. Kou, W. Li, X. Fan, K. M. Unruh, J. G. Chen, J. Q. Xiao, *Angew. Chem. Int. Ed.* **2011**, *50*, 6847.

[2] W. Guo, K. N. Hui, K. S. Hui, *Mater. Lett.* **2013**, *92*, 291.

[3] a) I. Sta, M. Jlassi, M. Hajji, H. Ezzaouia, *Thin Solid Films* **2014**, *555*, 131; b) D. Luca, B. Gerrit, H. Anders, H. Leif, *J. Phys. Chem. C* **2014**, *118*, 19556; c) K. Matsubara, S. Huang, M. Iwamoto, W. Pan, *Nanoscale* **2014**, *6*, 688.

[4] a) J. S. Choi, H. Y. Lee, K. H. Kim, *J. Phys. Chem.* **1973**, *77*, 2430; b) A. Kuzmin, N. Mironova, *J. Phys.: Condens. Matter.* **1998**, *10*, 7937; c) A. Kuzmin, N. Mironova, J. Purans, A. Rodionov, *J. Phys.: Condens. Matter.* **1995**, *7*, 9357.

[5] Z. G. Yang, L. P. Zhu, Y. M. Guo, Z. Z. Ye, B. H. Zhao, *Thin Solid Films* **2011**, *519*, 5174.

[6] J. W. Mares, R. C. Boutwell, M. Wei, A. Scheurer, W. V. Schoenfeld, *Appl. Phys. Lett.* **2010**, *97*, 161113.

[7] a) X. H. Xia, J. P. Tu, X. L. Wang, C. D. Gu, X. B. Zhao, *J. Mater. Chem.* **2011**, *21*, 671; b) X. H. Xia, J. P. Tu, J. Zhang, X. L. Wang, W. K. Zhang, H. Huang, *Sol. Energy Mater. Sol. Cells* **2008**, *92*, 628.

[8] a) M. M. Uplane, S. H. Mujawar, A. I. Inamdar, P. S. Shinde, A. C. Sonavane, P. S. Patil, *Appl. Surf. Sci.* **2007**, *253*, 9365; b) G. F. Cai, J. P. Tu, J. Zhang, Y. J. Mai, Y. Lu, C. D. Gu, X. L. Wang, *Nanoscale* **2012**, *4*, 5724.

[9] a) W. S. Yan, Z. H. Sun, Z. R. Li, Q. H. Liu, T. Yao, Z. Y. Pan, C. Wang, F. C. Hu, Y. Jiang, Z. M. Qi, F. Zeng, S. Q. Wei, *Adv. Mater.* **2012**, *24*, 353; b) M. D. Irwin, J. D. Servaites, D. Bruce Buchholz, B. J. Leever, J. Liu, J. D. Emery, M. Zhang, J.-H. Song, M. F. Durstock, A. J. Freeman, M. J. Bedzyk, M. C. Hersam, R. P. H. Chang, M. A. Ratner, T. J. Marks, *Chem. Mater.* **2011**, *23*, 2218; c) E. D. Gaspera, M. Guglielmi, S. Agnoli, G. Granozzi, M. L. Post, V. Bello, G. Mattei, A. Martucci, *Chem. Mater.* **2010**, *22*, 3407.

[10] a) P. Arumugam, D. Patra, B. Samanta, S. S. Agasti, C. Subramani, V. M. Rotello, *J. Am. Chem. Soc.* **2008**, *130*, 10046; b) J. Wang, D. Wang, N. S. Sobal, M. Giersig, M. Jiang, H. Möhwald, *Angew. Chem. Int. Ed.* **2006**, *45*, 7963; c) C. Y. Zhang, X. J. Zhang, X. H. Zhang, X. M. Ou, W. F. Zhang, J. S. Jie, J. C. Chang, C. S. Lee, S. T. Lee, *Adv. Mater.* **2009**, *21*, 4172; d) S. Biswas, L. T. Drzal, *Nano Lett.* **2008**, *9*, 167; e) L. F. Hu, R. Ma, T. C. Ozawa, T. Sasaki, *Angew. Chem. Int. Ed.* **2009**, *48*, 3846.

[11] a) F. Reincke, S. G. Hickey, W. K. Kegel, D. Vanmaekelbergh, *Angew. Chem., Int. Ed.* **2004**, *43*, 458; b) Y. J. Li, W. J. Huang, S. G. Sun, *Angew. Chem. Int. Ed.* **2006**, *45*, 2537; c) Y. Lin, H. Skaff, T. Emrick, A. D. Dinsmore, T. P. Russell, *Science* **2003**, *299*, 226; d) H. W. Duan, D. Y. Wang, D. G. Kurth, H. Möhwald, *Angew. Chem. Int. Ed.* **2004**, *43*, 5639; e) L. F. Hu, M. Chen, X. S. Fang, L. M. Wu, *Chem. Soc. Rev.* **2012**, *41*, 1350.

[12] a) A. E. Saunders, P. S. Shah, M. B. Sigman Jr., T. Hanrath, H. S. Hwang, K. T. Lim, K. P. Johnston, B. A. Korgel, *Nano Lett.* **2004**, *4*, 1943; b) A. Stein, B. E. Wilson, S. G. Rudisill, *Chem. Soc. Rev.* **2013**, *42*, 2763; c) H. Y. Wei, J. H. Huang, C. Y. Hsu, F. C. Chang, K. C. Ho, C. W. Chu, *Energy Environ. Sci.* **2013**, *6*, 1192; d) L. F. Hu, M. Chen, W. Z. Shan, T. R. Zhan, M. Y. Liao, X. S. Fang, X. H. Hu, L. M. Wu, *Adv. Mater.* **2012**, *24*, 5872; e) L. F. Hu, L. M. Wu, M. Y. Liao, X. S. Fang, *Adv. Mater.* **2011**, *23*, 1988.

[13] a) Y. H. Cho, G. Cho, J. S. Lee, *Adv. Mater.* **2004**, *16*, 1814; b) J. M. McLellan, M. Geissler, Y. Xia, *J. Am. Chem. Soc.* **2004**, *126*, 10830; c) Z. Niu, J. He, T. P. Russell, Q. Wang, *Angew. Chem. Int. Ed.* **2010**, *49*, 10052; d) R. Gao, L. F. Hu, M. Chen, L. M. Wu, *Small*

2014, *10*, 3038; e) H. Chen, L. F. Hu, X. S. Fang, L. M. Wu, *Adv. Funct. Mater.* **2012**, *22*, 1229; f) C. Li, G. S. Hong, L. M. Qi, *Chem. Mater.* **2010**, *22*, 476.

[14] D. C. Pan, X. L. Wang, Z. H. Zhou, W. Chen, C. L. Xu, Y. F. Lu, *Chem. Mater.* **2009**, *21*, 2489.

[15] a) X. S. Fang, L. F. Hu, K. F. Huo, B. Gao, L. J. Zhao, M. Y. Liao, P. K. Chu, Y. Bando, D. Golberg, *Adv. Funct. Mater.* **2011**, *21*, 3907; b) X. Wang, M. Y. Liao, Y. T. Zhong, J. Y. Zheng, W. Tian, T. Y. Zhai, C. Y. Zhi, Y. Ma, J. N. Yao, Y. Bando, D. Golberg, *Adv. Mater.* **2012**, *24*, 3421.

[16] a) R. W. Godby, M. Schlüter, L. J. Sham, *Phys. Rev. B* **1988**, *37*, 10159; b) M. S. Hybertsen, S. G. Louie, *Phys. Rev. B* **1986**, *34*, 5390.

[17] T. Zhu, S. P. Gao, *J. Phys. Chem. C* **2014**, *118*, 11385.

[18] a) Z. X. Wang, M. Safdar, C. Jiang, J. He, *Nano Lett.* **2012**, *12*, 4715; b) T. Y. Zhai, X. S. Fang, M. Y. Liao, X. J. Xu, L. Li, B. D. Liu, Y. Koide, Y. Ma, J. N. Yao, Y. Bando, D. Golberg, *ACS Nano* **2010**, *4*, 1596; c) T. Y. Zhai, H. M. Liu, H. Q. Li, X. S. Fang, M. Y. Liao, L. Li, H. S. Zhou, Y. Koide, Y. Bando, D. Golberg, *Adv. Mater.* **2010**, *22*, 2547.

[19] Y. M. Zhao, J. Y. Zhang, D. Y. Jiang, C. X. Shan, Z. Z. Zhang, B. Yao, D. X. Zhao, D. Z. Shen, *J. Phys. D: Appl. Phys.* **2009**, *42*, 092007.

[20] a) X. Li, F. Tao, Y. Jiang, Z. Xu, *J. Colloid. Interface Sci.* **2007**, *308*, 460; b) I. Rodriguez, F. Ramiro-Manzano, P. Atienzar, J. M. Martinez, F. Meseguer, H. Garcia, A. Corma, *J. Mater. Chem.* **2007**, *17*, 3205; c) X. Chen, J. Ye, S. Ouyang, T. Kako, Z. Li, Z. Zou, *ACS Nano* **2011**, *5*, 4310.

[21] Z. W. Deng, M. Chen, G. X. Gu, L. M. Wu, *J. Phys. Chem. B* **2008**, *112*, 16.

[22] S. J. Clark, M. D. Segall, C. J. Pickard, P. J. Hasnip, M. J. Probert, K. Refson, M. C. Payne, *Z. Kristallogr.* **2005**, *220*, 567.